Petroleum Science 23 (2026) 5111–5128

Contents lists available at ScienceDirect

Petroleum Science

journal homepage: www.keaipublishing.com/en/journals/petroleum-science

Original Paper

Ultrasonic velocity-based model for water holdup prediction in polymer-oil-water flows

Feng Yue, Lan-Di Bai *, Jia-Chen Zhang, Zi-Yan Tang, Ning-De Jin

School of Electrical and Information Engineering, Tianjin University, Tianjin, 300072, China

A R T I C L E I N F O

Article history:
Received 8 October 2025
Received in revised form
14 December 2025
Accepted 3 April 2026
Available online 6 April 2026

Edited by Xi Zhang

Keywords:
Polymer-containing oil-water two-phase flow
Flow pattern transition mechanism
Ultrasonic velocity measurement
Improved interfacial momentum transfer model
Water holdup prediction

A B S T R A C T

Polymer flooding significantly enhances crude oil recovery, but its complex rheological properties pose challenges to traditional water holdup measurement. We conduct experimental studies in a 20-mm vertical upward pipe. this work studies ultrasonic propagation in polymer-containing oil-water flows and evaluates different water holdup prediction models. Experiments were conducted using industrial white oil and 200 ppm and 1000 ppm Non-ionic polyacrylamide solutions (NIPAS), covering flow velocities of 5–12 m/day and water cuts of 10%–98%. Signals were synchronously acquired via high-speed camera and ultrasonic sensors, identifying five flow patterns: very fine dispersed oil in water (VFD O/W), dispersed oil in water (D O/W), dispersed large oil bubble in water (D LO/W), dispersed oil slug (D OS/W) and dispersed elongated oil slug (D EOS/W). Combined Weber number (We) and Ohnesorge number (Oh) analysis revealed that viscous forces dominate flow pattern transition at high polymer concentrations. The proposed improved interfacial momentum transfer (IIMT) model introduces a time-harmonic vibration assumption, transforms the dispersed-phase force balance into the frequency domain, and derives the equivalent mixture density through control-volume momentum analysis, establishing a physical relationship between sound velocity and water holdup. This framework effectively bridges microscopic droplet oscillations with the macroscopic acoustic response, providing a unified prediction approach for complex flow patterns. Experimental results demonstrate the high predictive accuracy of the IIMT model, achieving an average absolute deviation (AAD) of 0.0154 and an average absolute percentage deviation (AAPD) of 2.49% at 200 ppm, and an AAD of 0.0145 with an AAPD of 2.06% at 1000 ppm. This performance robustly validates the effectiveness and innovation of the interfacial momentum transfer model proposed in this study.

1. Introduction

In recent years, polymer flooding technology has been widely used in Chinese oilfields to enhance oil recovery, primarily by improving the sweep efficiency of injected water. Meanwhile, the complex rheological behavior of polymer-containing oil-water two-phase flow has become an important topic in multiphase flow research (Lamas et al., 2021; Seright and Brattekas, 2021; Navaie et al., 2022; Seright and Wang, 2023; Wang et al., 2024). The addition of polymers significantly alters the viscosity, surface tension, turbulence structure (Bai et al., 2022; Rosado-Vázquez et al., 2022; Tan et al., 2022), phase distribution, and interfacial slip effects (Clarke et al., 2016; Zhong et al., 2018; Chen et al., 2023) of the system, thereby leading to considerable deviations in water holdup prediction. Therefore, identifying the flow patterns of oil-water two-phase flow under the influence of polymers, establishing an ultrasonic velocity model suitable for polymer-containing multiphase flows, and elucidating the influence mechanism of polymer concentration on flow pattern evolution and acoustic signals are of great theoretical and engineering significance for improving the accuracy of water holdup measurement.

As a non-contact measurement method, ultrasonic detection is widely used in multiphase flow parameter detection due to its advantages of non-invasiveness and high sensitivity (Zhang et al., 2019; Zhao et al., 2016; Lu et al., 2021; Xie et al., 2024). Xu et al.

* Corresponding author.
E-mail address: bld_27@tju.edu.cn (L.-D. Bai).

Peer review under the responsibility of China University of Petroleum (Beijing).

https://doi.org/10.1016/j.petsci.2026.04.004

Nomenclature

c	Speed of ultrasound in the medium, m/s
D	Pipe inner diameter, m
f	Ultrasonic frequency, Hz
F	Force, N
F_A	Added mass force, N
F_B	Basset (history) force, N
F_G	Gravitational force, N
F_P	Pressure gradient force, N
F_{Stokes}	Stokes viscous drag force, N
g	Gravitational acceleration, m/s^2
k	Complex propagation constant, m^{-1}
m	Embedding dimension
M'	Momentum flux per unit volume, kg/(m^2·s)
N	Number of signal sampling points, N
R	Droplet radius, m
u	Volumetric flux velocity, m/s
u_o	Oil phase velocity, m/s
u_w	Water phase velocity, m/s
U_m	Mixture velocity, m/s
Y_o	Oil phase volume fraction
Y_w	Water phase volume fraction
β	Bulk modulus of elasticity, Pa
κ_o	Oil phase adiabatic compressibility, Pa^{-1}
κ_w	Water phase adiabatic compressibility, Pa^{-1}
λ	Wavelength, m
μ_o	Oil phase viscosity, Pa·s
μ_w	Water phase viscosity, Pa·s
μ_m	Mixture viscosity, Pa·s
ρ_o	Oil density, kg/m^3
ρ_w	Water density, kg/m^3
ρ_m	Mixture density, kg/m^3
σ	Surface tension, N/m
τ	Time delay, s
ω	Angular frequency of ultrasound, rad/s
AAD	Average absolute deviation
AAPD	Average absolute percentage deviation
VFD O/W	Very fine dispersed oil in water
D O/W	Dispersed oil in water flow pattern
D LO/W	Dispersed large oil bubble in water
D OS/W	Dispersed oil slug in water
D EOS/W	Dispersed elongated oil Slug in water
Re	Reynolds number
Oh	Ohnesorge number
We	Weber number
NIPAS	Non-ionic polyacrylamide solution

(1985) used opposed ultrasonic sensors to measure the gas concentration in gas-liquid two-phase flow, pointing out that pulsed ultrasound can suppress standing waves and enable fluid characterization through peak detection. Bonnet and Tavlarides (1987) proposed an ultrasonic holdup measurement method based on average propagation time applicable to liquid-liquid two-phase flow systems. Subsequently, many scholars have studied the relationships between ultrasonic attenuation/sound velocity and dispersed-phase concentration, particle size, and flow patterns (Stolojanu and Prakash, 1997; Zheng and Zhang, 2004; Carvalho et al., 2009; Rahiman et al., 2013). In previous research by our group, Zhai et al. (2013) found through numerical simulation that the sound pressure level is highly sensitive to the dispersed-phase concentration; Ren et al. (2022) established a gas holdup measurement model based on bubble diameter, indicating that selecting an appropriate bubble diameter helps improve the measurement accuracy of gas holdup in oil-gas-water three-phase flow.

Inverting phase fraction by measuring ultrasound propagation velocity offers real-time capability and reliability. The fundamental relation between sound velocity and medium density and adiabatic compressibility was established by Wood (1930). Urick later proposed the classic model (Urick, 1947; Urick and Ament, 1949), treating a suspension or emulsion as a homogeneous "pseudo-fluid" whose sound velocity is the linear volume-weighted average of its constituents' properties. This model assumes the dispersed phase is much smaller than the acoustic wavelength, thereby neglecting scattering, interfacial forces, viscous dissipation, particle size distribution, and flow structures. Fan and Wang (2021) categorize it as a representative "coupled phase model" for uniform systems, noting its limitations at high frequencies or with large particles. Yang et al. (2023) further demonstrated significant prediction deviations when particles are non-uniformly distributed, especially at high frequencies.

The interphase momentum transfer (IMT) model (Basset, 1888; Tchen, 1947; Hinze, 1959; Zuber, 1964; Harker and Temple, 1988) departs from the ideal "homogeneous mixture" assumption by analyzing interfacial forces on a dispersed particle (Stokes, 1851; Boussinesq, 1903) to establish its dynamic equation. It posits that during acoustic propagation, relative motion occurs between phases, subjecting particles to forces such as Stokes drag, added mass, Basset (history), and pressure gradient forces. Solving this equation yields the interphase velocity response.

Key developments include that Tchen (1947) incorporating the pressure gradient into Basset's equation; Zuber (1964) modifying the added mass force for particle concentration; and Harker and Temple (1988) introducing an oscillatory Stokes drag and modified added mass for high-frequency ultrasound, formulating a frequency-domain velocity response for droplets in an acoustic field. Evans and Attenborough (1997) extended the coupled-phase theory to compressible, thermoviscous emulsions by including energy conservation and heat transfer, improving predictions of velocity and attenuation. Han et al. (2017) applied this framework to suspension-porous-solid interfaces, and Fang et al. (2025) integrated Harker's momentum transfer with Evans' thermo-mechanical coupling, proposing a full-wavelength model that accounts for thermoviscous and scattering losses, thereby enhancing accuracy and applicability in liquid-solid flows.

While existing models primarily describe acoustic propagation in emulsions with a focus on attenuation, polymer-containing oil-water flows exhibit distinct properties. The primary objective of this study is to establish an ultrasonic water holdup prediction model suitable for polymer-containing oil-water two-phase flows. This research is based on the assumptions that droplets are uniform-sized rigid spherical bodies and the fluid behaves as a Newtonian fluid. The experiments were conducted in a vertical small-diameter pipe, with temperature variations neglected. Flow patterns can be effectively identified using PDF and RP methods. Building on this foundation, this paper proposes an improved interfacial momentum transfer (IIMT) model. For the first time, this model integrates the microscopic forced oscillation of droplets with the macroscopic acoustic velocity response through a control volume momentum conservation framework, thereby refining the calculation method for the equivalent density of the mixed medium. Simultaneously, by incorporating the We number and the Oh number, the model systematically elucidates the physical mechanisms underlying flow pattern transitions.

2. Experimental setup

The experiment established a setup for ultrasonic velocity measurement in vertical upward oil-water two-phase flow containing polymer in the Multiphase Flow Laboratory of Tianjin University. The experiment was conducted in a vertical upward pipe section with an inner diameter of 20 mm. The overall layout of the experimental system is shown in Fig. 1, where Fig. 1(a) shows the actual installation of the ultrasonic sensors and high-speed camera equipment.

2.1. Experimental system

The experimental apparatus mainly consists of three parts: the fluid circulation system, the measurement system, and the data acquisition system. The fluid circulation system includes a stirring tank, an oil storage tank, a mixing tank, high-precision industrial peristaltic pumps, and corresponding delivery pipelines. The two-phase fluids are transported by independent peristaltic pumps and injected into the vertical test section through a bottom mixer. After flowing through a 1700 mm long flow development section, the fluid enters the test area, passing sequentially through the high-speed camera observation window and the ultrasonic sensor measurement zone, before finally returning to the oil-water mixing tank for recycling. Temperature was strictly controlled during the experiment, and the sound velocity in pure media was used as a reference for calibration.

Fig. 1(b) is a schematic diagram of the sensor measurement system. The ultrasonic sensor system consists of an ultrasonic probe, a high-voltage pulse excitation module, a signal reception and conditioning module, and an FPGA-based USB data acquisition module. The ultrasonic probe is an Olympus 6 mm single-crystal immersion longitudinal wave probe with a center frequency of 2.25 MHz. The excitation signal is a 1 kHz high-voltage pulse generated by the FPGA, with a pulse width of about 0.44 μs. The reception system uses 40 MHz high-speed sampling. The received ultrasonic signal is amplified and filtered, then converted into a digital signal by a high-speed A/D module and transmitted to the host computer for storage and processing.

Prior to conducting two-phase flow experiments, the ultrasonic measurement system was calibrated. Pure water and pure oil were injected separately into the pipeline. The propagation time of ultrasonic waves along a fixed acoustic path equal to the pipe diameter of 20 mm was measured, and calibration was performed based on the known sound velocities of pure water (approximately 1500 m/s) and pure oil (approximately 1340 m/s) at 26 °C. This calibration procedure was repeated daily before experiments to correct for potential temporal drift in the system, ensuring the baseline accuracy of sound velocity measurements.

The flow patterns were visually observed using a high-speed camera. The camera was positioned outside a transparent observation window at the test section. All experiments were recorded at a frame rate of 1000 fps and a resolution of 1280 × 1024 pixels. A high-intensity LED backlight provided uniform illumination, ensuring clear contrast between the oil and water phases.

For each flow condition, the experimental water holdup values were obtained using a quick closing valve (QCV) assembly as a reference standard. Two pneumatically actuated ball valves,

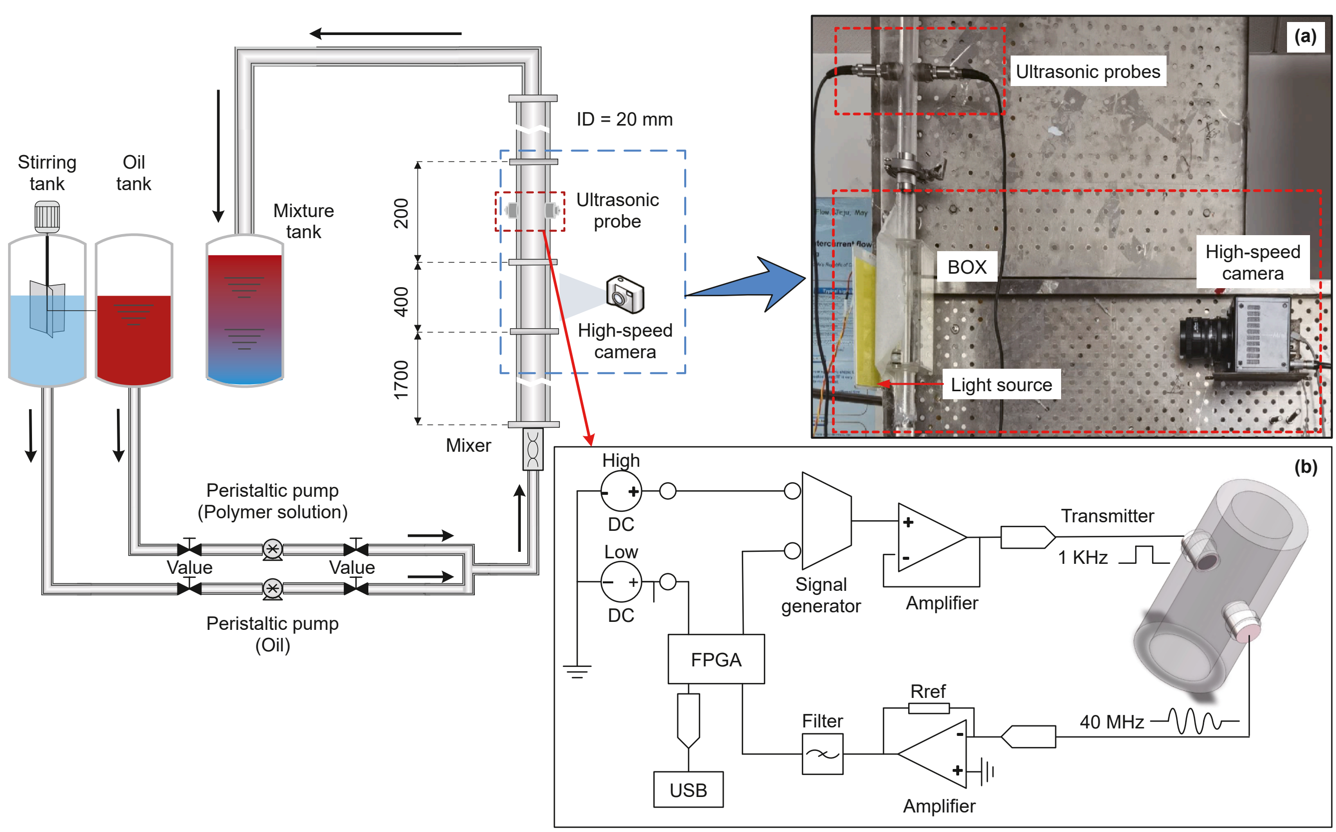

Fig. 1. Diagram of the experimental setup for polymer-containing vertical upward oil-water two-phase flow: (**a**) photograph of the experimental setup; (**b**) schematic of the sensor measurement system.

installed immediately upstream and downstream of the test section, were designed to close simultaneously within 30 ms after triggering. Subsequently, the volumes of oil and water were measured separately to calculate the water holdup. During this process, the closure time of the quick-closing valves was significantly shorter than the flow velocity of the two-phase mixture within the test section. Furthermore, the upstream and downstream valves were driven by a single actuator, ensuring synchronized operation and avoiding fluid displacement or loss due to asynchronous valve movement. This allowed the trapped sample to highly represent the instantaneous cross-sectional state under steady flow conditions, thereby providing a reliable benchmark for water holdup calculation.

The total flow rate range was set from 5 to 12 m^3/day, and the water cut varied from 10% to 98%. For each flow condition, flow images and ultrasonic sound velocity signals were synchronously acquired. The experimental water holdup value was obtained using a quick-closing valve device for subsequent comparative analysis with the model-predicted water holdup values.

2.2. Fluid media

Industrial No. 3 white oil was selected as the oil phase medium, with a density of 812 kg/m^3 and a viscosity of 3.82 mPa·s. The aqueous phase medium was a NIPAS prepared in a stirring tank. By adding 34 g and 170 g of polymer powder to 170 L of tap water, respectively, two solutions with concentrations of 200 ppm and 1000 ppm were obtained. The solutions were stirred in the tank at a rated speed for 2 h and then left to stand overnight to ensure complete hydrolysis and solution stability. To facilitate high-speed camera observation, the oil phase was dyed with Sudan Red.

The fluid parameters are shown in Table 1. At 26 °C, the densities of the two NIPAS at different concentrations were both approximately 998 kg/m^3, while the viscosity increased with increasing polymer concentration. The viscosities of the 200 ppm and 1000 ppm NIPAS were 0.93 mPa·s and 1.35 mPa·s, respectively, and the surface tensions were 0.074 N/m and 0.075 N/m, respectively. The oil phase, Industrial No. 3 white oil, had a density of 812 kg/m^3 and a viscosity of 3.82 mPa·s.

2.3. Uncertainty analysis

High-precision peristaltic pumps were used to deliver the oil and water phases, calibrated precisely using the volume-time method. Within the flow rate range, the flow error of a single pump did not exceed 0.2%.

The ultrasonic velocity measurement used a 40 MHz sampling clock, with a time resolution of 0.025 μs, leading to a maximum measurement error of 0.025 μs in the wave propagation time. Taking the sound velocity in pure water, the fastest propagating medium at 1500 m/s, as an example, the corresponding propagation time is 13.33 μs. Therefore, the maximum relative measurement error in sound velocity introduced by the time resolution does not exceed 0.19%.

Table 1
Density, viscosity and surface tension of the fluid media used in the experiment at 26 °C.

Fluid medium	Density ρ, kg/m^3	Viscosity μ, mPa·s	Surface tension σ, mN/m
200 ppm NIPAS	998	0.93	74
1000 ppm NIPAS	998	1.35	75
No. 3 Industrial white oil	812	3.82	33

In summary, the combined uncertainty of the measurement system can be calculated as:

$$u = \sqrt{(0.2\%)^2 + (0.2\%)^2 + (0.19\%)^2} \approx 0.34\% \tag{1}$$

This uncertainty originates mainly from the measurement accuracy of the flow rate and sound velocity. Its magnitude is much smaller than the variation range of water holdup in the experiment, indicating that the measurement precision of the experimental system can effectively capture subtle changes in flow parameters, meeting the requirements for subsequent flow pattern identification and water holdup model validation.

3. Flow patterns in polymer-containing oil-water two-phase flow

This study first measured the ultrasonic velocity in the NIPAS and in pure oil. As shown in Fig. 2, the sound velocity measured in the NIPAS was about 1500 m/s, and in pure oil about 1340 m/s. The sound velocities in both media remained stable over the 10-s measurement period without significant fluctuations, thus these values can be used as reference sound velocities for the respective media.

Figs. 3 and 4 show snapshots of the flow patterns and their corresponding sound velocity signals for concentrations of 200 ppm and 1000 ppm, respectively. Five flow patterns were identified in the experiments: VFD O/W, D O/W, D LO/W, D OS/W, and D EOS/W, with no continuous phase inversion occurring in any of them.

Fig. 3(a) shows the VFD O/W pattern, where the oil phase is distributed as finely dispersed droplets with high uniformity. The D O/W flow is characterized by upward-moving oil droplets of diverse sizes and structures within the water phase. In the D LO/W, large oil droplets coalesce into clusters, while fine oil droplets are dispersed in the water phase between the clusters. In the D OS/W, droplets coalesce into oil slugs occupying the entire cross-section, with clusters of oil droplets following behind the slug tail moving upward. In the D EOS/W, the intermittent upward movement of oil slugs and water slugs is also evident. Due to insufficient energy to sustain slug motion, the liquid film becomes highly unstable, leading to structural distortion. Consequently, the oil slugs undergo squeezing, elongation, and even pinch-off, ultimately resulting in rupture.

Figs. 3(b), 4(a)–(b) show the measurement results for the D O/W flow pattern. Compared to the VFD O/W pattern, the sound velocity signal fluctuations are significantly intensified. Combined with high-speed imaging, these fluctuations are primarily attributed to the presence of large oil bubbles, which noticeably affect the sound velocity. It is worth noting that under the same high flow velocity and high water cut conditions, a polymer concentration of 1000 ppm promotes oil phase coalescence compared to 200 ppm, leading to a transition from the VFD O/W to the D O/W flow pattern.

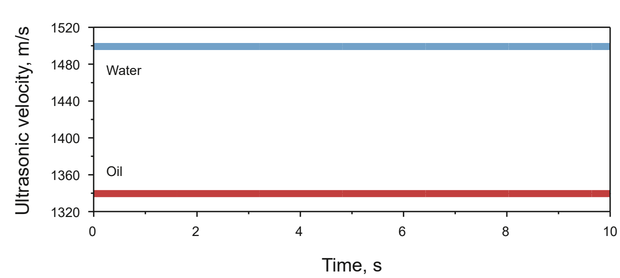

Fig. 2. Sound velocity signals in pure water and pure oil.

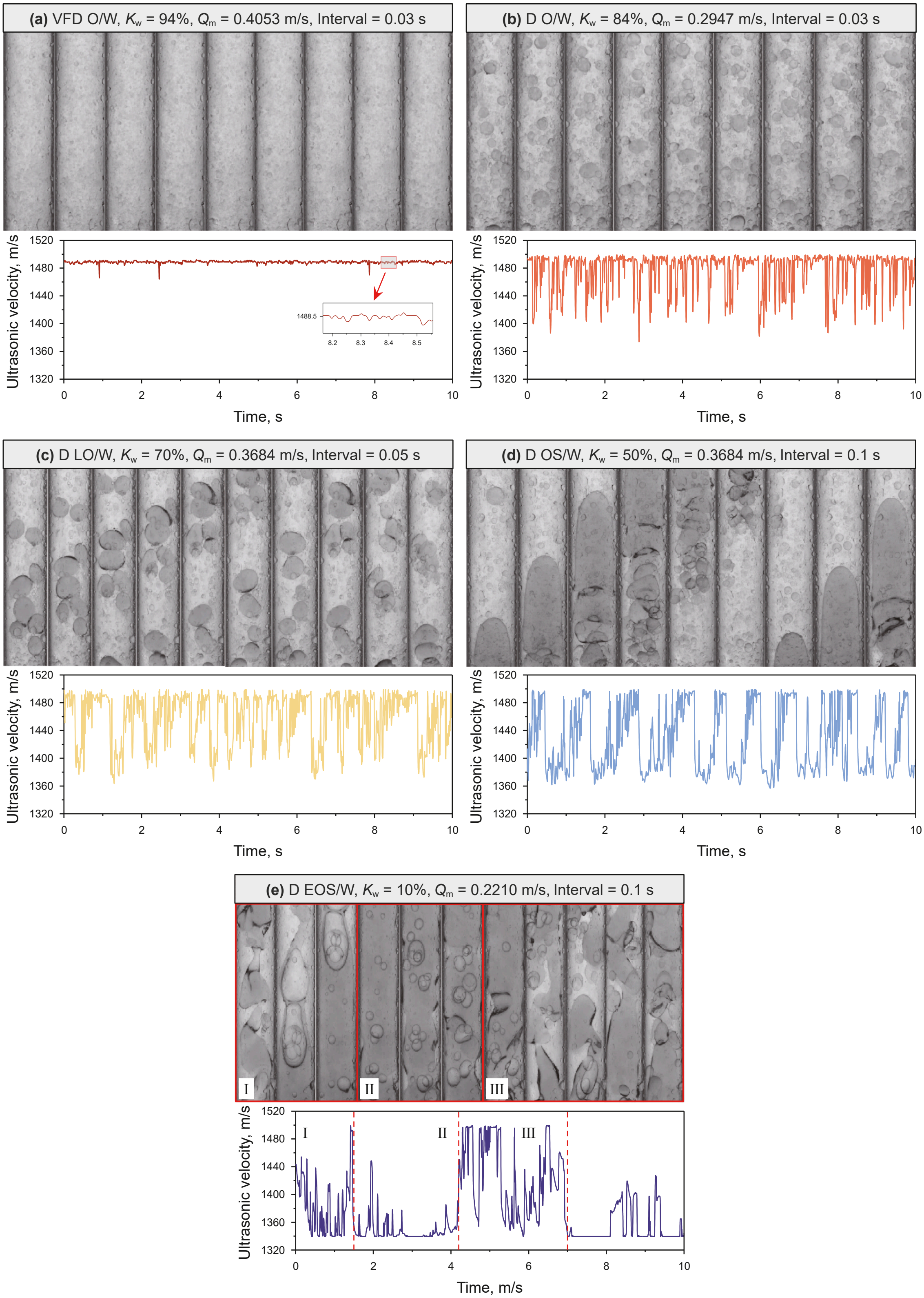

Fig. 3. Typical ultrasonic velocity signals and flow patterns in 200 ppm NIPAS: (**a**) VFD O/W; (**b**) D O/W; (**c**) D LO/W; (**d**) D OS/W; (**e**) D EOS/W.

Figs. 3(c) and 4(c) show the sound velocity signals for the D LO/W flow pattern. Their fluctuation characteristics are similar to those of the D O/W pattern, but the baseline changes are more severe and exhibit periodic jumps. High-speed imaging reveals that in this pattern, large oil droplets aggregate into clusters, while dispersed oil droplets of different sizes are still distributed among them.

Figs. 3(d) and 4(d) correspond to the D OS/W flow pattern. This pattern consists of alternating oil slugs and water slugs; therefore, the sound velocity signal exhibits typical alternating high and low

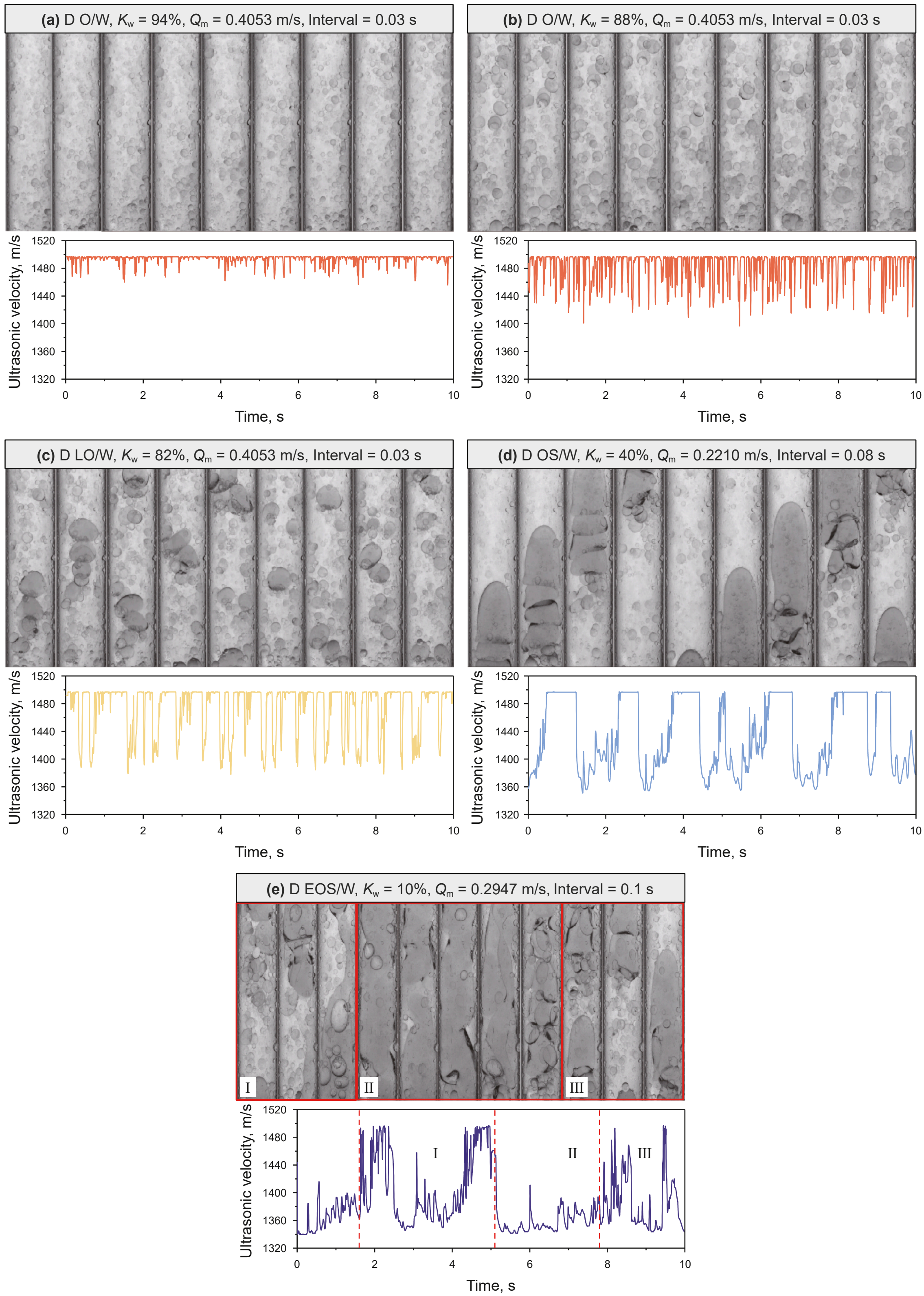

Fig. 4. Typical ultrasonic velocity signals and flow patterns in 1000 ppm NIPAS: (**a**) D O/W; (**b**) D O/W; (**c**) D LO/W; (**d**) D OS/W; (**e**) D EOS/W.

sound velocity phenomena. The images show a large number of large oil bubbles at the tail of the oil slug, connected to the following water slug, resulting in an initially low sound velocity signal during the oil slug stage accompanied by significant fluctuations.

Fig. 3(e) shows the high-speed camera images and sound velocity signals for the D EOS/W pattern at 200 ppm. Under conditions of low mixture velocity or water cut, the oil slug is elongated, velocity fluctuations in the vertical direction are large, liquid film instability is pronounced, the structure is distorted, and thickness changes frequently. Consequently, the sound velocity fluctuates violently around a lower baseline. Region I corresponds to the chaotic flow zone before the formation of the elongated slug, where the oil slug morphology is slender and continuously changing, leading to a complex sound velocity sequence. Region II is the main body of the elongated slug, where the oil slug fills the pipe, and frequent liquid film changes and detachment cause the sound velocity to jump upwards from the baseline of pure oil sound velocity. Region III is the stage after the elongated slug ends, where the flow first exhibits characteristics similar to a large bubble flow (with similar sound velocity behavior) before transitioning back to a complex state.

Fig. 4(e) shows the observations for the D EOS/W pattern at 1000 ppm. The sound velocity still fluctuates violently around a low baseline, similar to the 200 ppm case, and structural instability and rupture due to liquid film detachment and squeezing of the oil slug are still present. Regions I and III represent the sections before and after the elongated slug, respectively. The higher polymer concentration intensifies oil phase coalescence, causing these regions to exhibit alternating oil and water slug flow, and even phenomena like squeezing, elongation, or breakup of oil slugs, resulting in complex acoustic signals. Region II is the elongated slug segment, with characteristics consistent with the 200 ppm case: the oil slug fills the pipe, and dynamic changes and detachment of the liquid film cause the sound velocity to continuously jump upwards near the pure oil baseline value.

4. Physical mechanism of flow pattern transition

To more intuitively analyze the flow conditions under different polymer concentrations, two dimensionless parameters, the We and the Oh, are introduced:

$$\mathrm{We} = \frac{\rho_{\mathrm{m}} U_{\mathrm{m}}^2 D}{\sigma} \tag{2}$$

$$\mathrm{Oh} = \frac{\mu_{\mathrm{m}}}{\sqrt{\rho_{\mathrm{m}} \sigma D}} = \frac{\mathrm{We}^{0.5}}{\mathrm{Re}} \tag{3}$$

where μ_{m} is the mixture viscosity, ρ_{m} is the mixture density, U_{m} is the mixture velocity, σ is the surface tension, D is the pipe diameter, and Re is the Reynolds number.

The Weber number measures the relative importance of inertial forces to surface tension in fluid flow. A higher value indicates that inertial forces dominate, making the flow more inclined to break oil droplets into smaller ones. The Ohnesorge number is a dimensionless parameter that comprehensively reflects the effects of viscous force, inertial force, and surface tension. A higher Oh value represents stronger viscous effects, which significantly inhibit droplet deformation and breakup.

Fig. 5 shows the joint distribution of the Weber number and Ohnesorge number for polymer concentrations of 200 ppm and 1000 ppm, respectively. It can be clearly seen that different flow patterns distribute in different regions of the dimensionless parameter space, showing obvious regularity. At the 1000 ppm concentration, the Oh number overall increases compared to the 200 ppm case, indicating that the increase in polymer concentration leads to higher mixture viscosity, thus increasing the Ohnesorge number.

The VFD O/W and D O/W flow patterns appear in the low Oh number region. Here, inertial forces and surface tension dominate, and the oil phase is broken into fine droplets under strong turbulent action, primarily forming these two flow patterns. It is noteworthy that VFD O/W only occurs under 200 ppm conditions and is located in the region of very high We number and very low Oh number, indicating that extremely high turbulent kinetic energy is a necessary condition for maintaining the ultra-fine dispersed state. When the polymer concentration increases to 1000 ppm, the increased solution viscosity leads to a significant increase in the Oh number, suppressing the turbulent breakup capability, thus causing the VFD O/W flow pattern to disappear.

The D LO/W flow pattern appears in the medium Oh number region. Here, the role of viscous forces strengthens, inertial forces weaken, and turbulence intensity decreases. At this point, surface tension and inertial forces tend to balance, and droplet breakup and coalescence phenomena coexist. The flow pattern manifests as oil droplets aggregating into clusters, accompanied by a transitional structure with some dispersed droplets.

In the high Oh number region, viscous forces absolutely dominate, inertial forces further weaken, and turbulence is significantly suppressed. Surface tension can no longer maintain the droplet morphology. The oil phase continuously coalesces and turbulence cannot break it up, subsequently forming oil slugs, and the flow pattern develops into D OS/W and D EOS/W.

5. Flow pattern identification for polymer-oil-water two-phase flow

5.1. Probability density function (PDF)

The probability density function (PDF), as a statistical method, is often used to analyze the probability distribution characteristics of time-domain signals. The PDF describes the probability that a random variable falls within a certain value range. For a sampled signal of length N, if N_0 points fall within the interval $[x, x+\Delta x]$, the probability density p_{d} within that interval is:

$$p_{\mathrm{d}} = \frac{N_0/N}{\Delta x} \tag{4}$$

The probability density function of the signal can then be expressed as:

$$\mathrm{PDF} = \lim_{\Delta x \to 0} p_{\mathrm{d}} \tag{5}$$

Fig. 6 shows the PDF distributions for the aforementioned flow conditions. It can be observed that the PDF for the VFD O/W flow pattern exhibits a narrow and high distribution, indicating that the oil droplets are fine and uniformly dispersed. The PDF for the D O/W flow pattern is a broad unimodal distribution, suggesting an uneven size distribution of oil droplets, causing the sound velocity to fluctuate over a wide range. At 1000 ppm, the peak position is closer to the sound velocity in pure water, indicating a larger average oil droplet size. The PDF for the D LO/W flow pattern shows a main peak in the high sound velocity region and a shoulder or secondary peak in the low sound velocity region, reflecting the characteristic coexistence of large oil droplets and dispersed droplets. The D OS/W pattern shows a significant bimodal distribution, corresponding to the periodic alternation of oil slugs (low sound velocity) and water slugs (high sound velocity). The PDF for the D EOS/W flow pattern is also bimodal, but the low sound velocity peak is higher and wider, and the distribution in the high sound velocity region is scattered, indicating that oil slugs persist for a longer time, and instability and rupture of the liquid film cause severe fluctuations in the sound velocity within the water slug region.

It is noteworthy that the right peak position of the sound velocity PDF at the 1000 ppm polymer concentration is significantly closer to the sound velocity value in pure water compared to the 200 ppm case. This is because the enhanced viscoelasticity of the high-concentration NIPAS inhibits oil flow breakup, promotes the coalescence of fine oil droplets, leads to increased spacing and

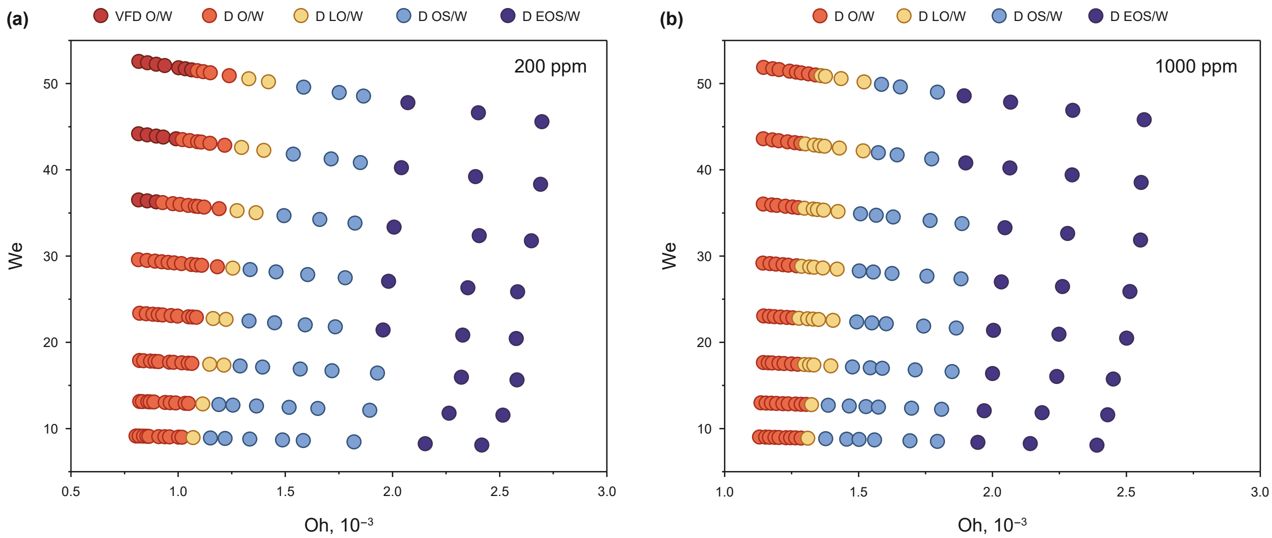

Fig. 5. Joint distribution map of Weber number and Ohnesorge number.

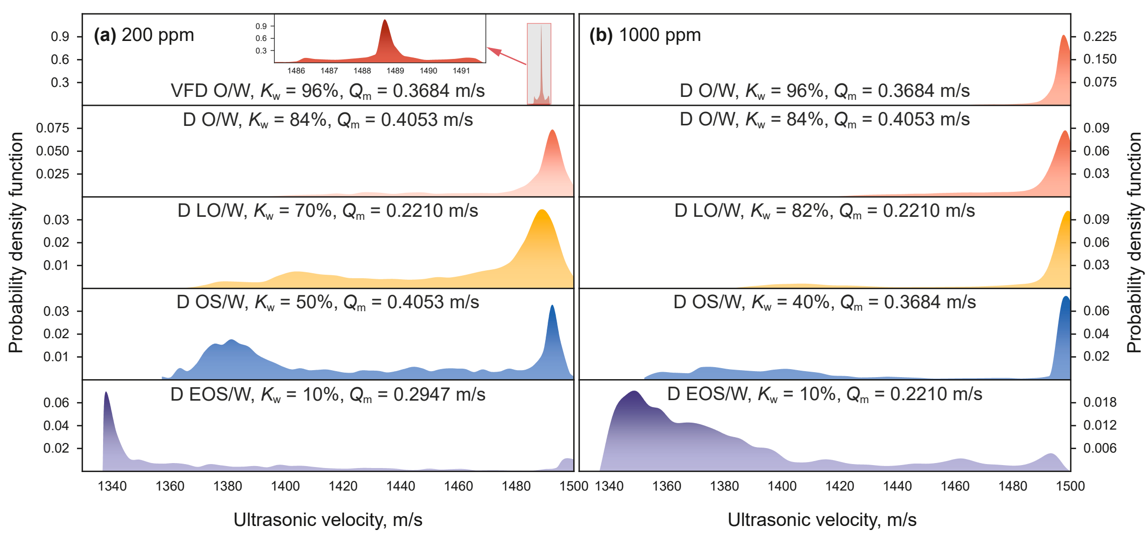

Fig. 6. Probability density function distributions based on sound velocity time series.

reduced number of dispersed phase droplets, making the sound velocity of the mixture closer to that in pure water.

5.2. Recurrence plot (RP)

The recurrence plot (RP) method (Takens, 1981; Eckmann et al., 1987) is used to directly observe the dynamics over time of trajectories $\mathbf{X}_i \in R^n (i = 1, \ldots, N)$ in an n-dimensional phase space. It is particularly suitable for revealing periodicities, transient behaviors, and chaotic characteristics in complex flows. It is basically defined by calculating an $N \times N$ matrix:

$$R_{i,j} = \Theta\left(\varepsilon - \|\mathbf{X}_i - \mathbf{X}_j\|\right), i,j = 1, \ldots N \tag{6}$$

where $||\mathbf{X}_i - \mathbf{X}_j||$ is the Euclidean norm; Θ is the Heaviside function; ε is a threshold, written as $\varepsilon = \alpha \cdot \mathrm{std}(s_i)$, where $\mathrm{std}(s_i)$ is the standard deviation of the original time series, and α is an empirical coefficient. For a one-dimensional time series, according to Takens' embedding theorem, the phase space vector is reconstructed using the time delay method:

$$\mathbf{X}_i = [s_i, s_{i+\tau} \ldots s_{i+(m-1)\tau}] \tag{7}$$

The threshold τ defines a sphere centered at $\mathbf{X}_j$. If $\mathbf{X}_j$ falls within this sphere, it means that this state is close to $\mathbf{X}_i$, thus set $R_{ij} = 1$, and plot a point (recurrence point) at the corresponding position (i, j) on the $N \times N$ coordinate plane. This yields a recurrence plot of the time series after phase space reconstruction.

Figs. 7 and 8 show the sound velocity signals and corresponding recurrence plots for typical flow patterns at polymer concentrations of 200 ppm and 1000 ppm, respectively. Fig. 7(a) shows the recurrence plot corresponding to the VFD O/W flow pattern. The recurrence points are fine and uniformly distributed, indicating that the sound velocity sequence is close to a stationary random process, consistent with the uniformly mixed nature of the fluid in this flow pattern. Figs. 7(b) and 8(a)–(b) correspond to the D O/W flow pattern. The recurrence plots show short diagonal line cluster structures, reflecting that the sound velocity fluctuations caused by oil bubbles have a certain degree of correlation. Figs. 7(c) and 8(c) show the recurrence plot results for the D LO/W flow pattern, where the diagonal line clusters are longer, indicating

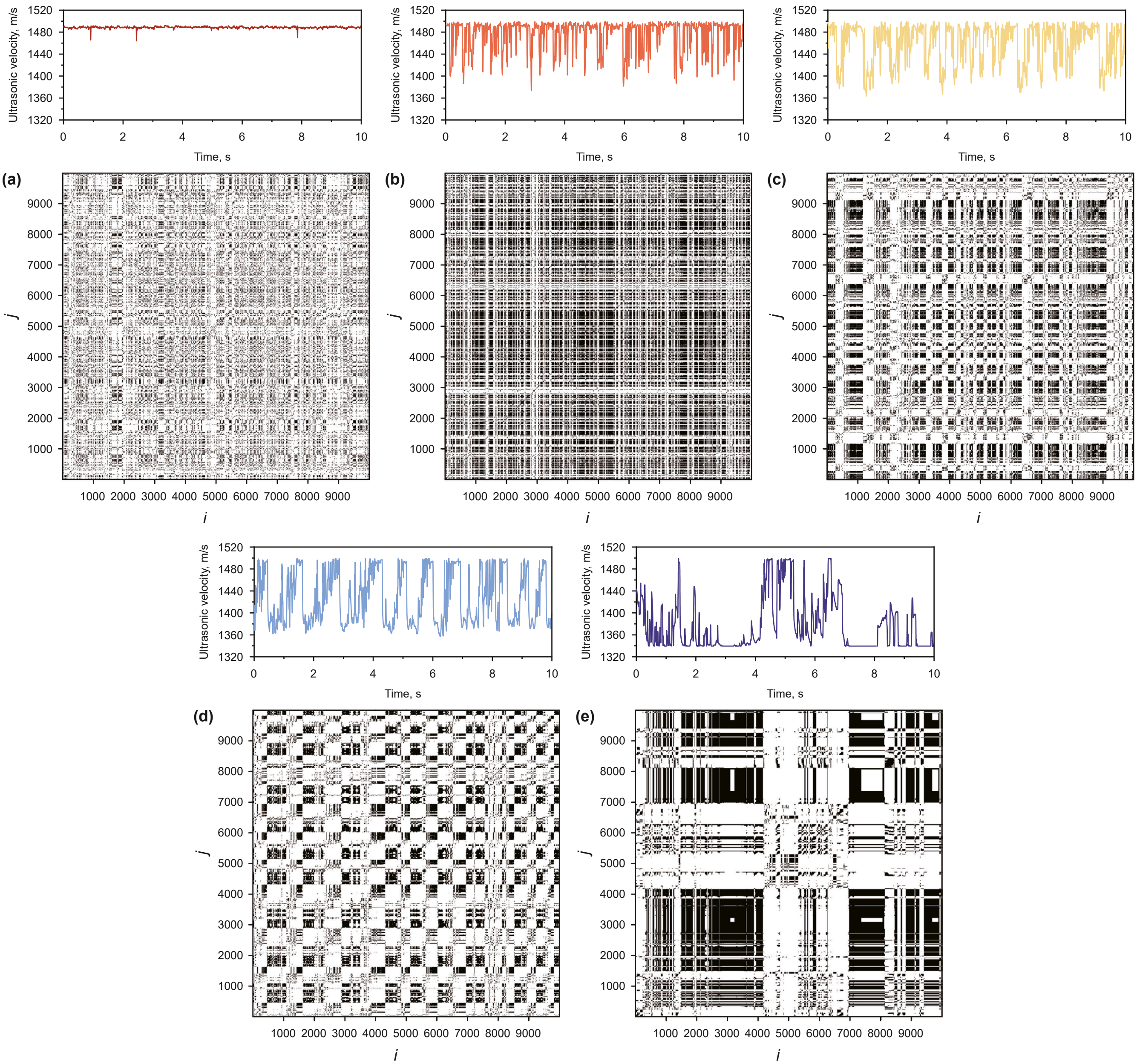

Fig. 7. Sound velocity sequences and recurrence plots at 200 ppm: (**a**) VFD O/W; (**b**) D O/W; (**c**) D LO/W; (**d**) D OS/W; (**e**) D EOS/W.

periodic coalescence behavior of oil droplet clusters under the influence of the polymer. Furthermore, the diagonal clusters at the 1000 ppm concentration are more concentrated than those at 200 ppm, indicating that the higher polymer concentration enhances oil droplet coalescence ability, reduces the generation of small oil bubbles, thereby causing the fluctuations of the sound velocity signal to tend to weaken.

Figs. 7(d) and 8(d) show the recurrence plots corresponding to the D OS/W flow pattern, presenting a regular grid-like pattern, reflecting the strong periodic characteristic of alternating oil slugs and water slugs. Figs. 7(e) and 8(e) are the recurrence plots for the D EOS/W flow pattern, which also show a grid-like structure but on a larger scale, reflecting the behavior of alternating elongated slugs and water slugs; simultaneously, within the grids corresponding to the periods before and after the oil slug, scattered points and short diagonal clusters are mixed, indicating the chaotic flow state caused by liquid film instability. The grids corresponding to the oil slug appear as long diagonal clusters, indicating that when the oil slug fills the pipe, the sound velocity undergoes continuous jumps due to liquid film detachment.

6. Physical model for predicting water holdup from ultrasonic velocity

The velocity of a small-amplitude plane wave propagating through solid, liquid, or gaseous media is determined solely by the elasticity and density of the medium it passes through, namely (Wood, 1930):

$$c = \sqrt{\frac{\beta}{\rho}} = \frac{1}{\sqrt{\kappa\rho}} \tag{8}$$

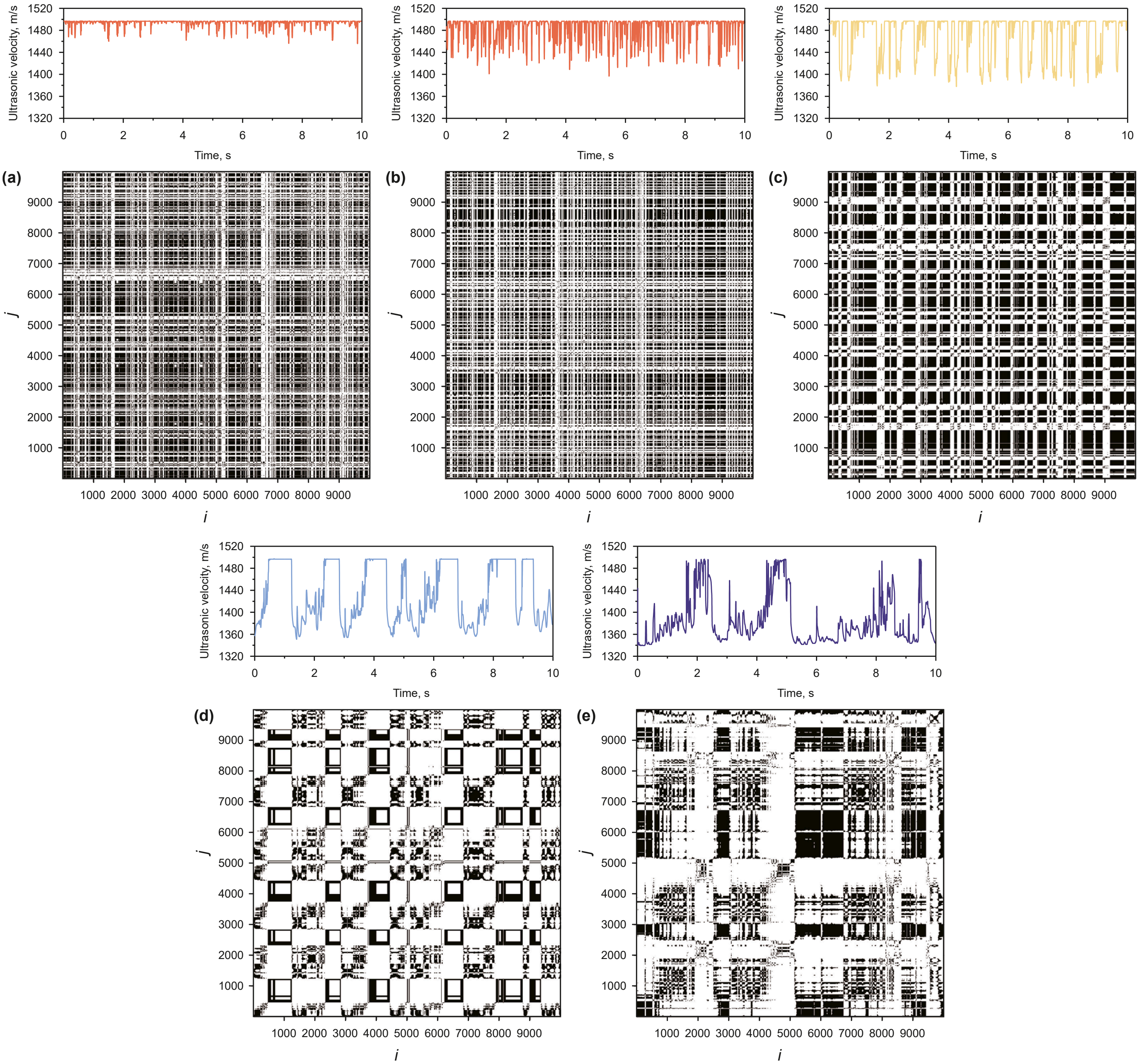

Fig. 8. Sound velocity sequences and recurrence plots at 1000 ppm: (**a**) D O/W; (**b**) D O/W; (**c**) D LO/W; (**d**) D OS/W; (**e**) D EOS/W.

where c is the sound velocity; κ is the adiabatic compressibility; β is the bulk elastic modulus; ρ is the density.

6.1. Urick model

Urick, in 1947, proposed a classic sound velocity prediction model suitable for suspensions and emulsions. It assumes that the suspension or emulsion is uniformly mixed and that the size of the dispersed phase is much smaller than the acoustic wavelength, neglecting sound velocity fluctuations due to non-uniform distribution of dispersed particles. The density and adiabatic compressibility of the mixture are the linear volume-weighted averages of the water and oil phases:

$$\rho = Y_\mathrm{W}\rho_\mathrm{W} + (1 - Y_\mathrm{W})\rho_\mathrm{O} \tag{9}$$

$$\kappa = Y_\mathrm{W}\kappa_\mathrm{W} + (1 - Y_\mathrm{W})\kappa_\mathrm{O} \tag{10}$$

where Y_W is the water holdup, ρ_W and ρ_O represent the water and oil phase densities, respectively, k_W and k_O represent the adiabatic compressibilities of the water and oil phases, respectively, and ρ and κ represent the equivalent density and equivalent adiabatic compressibility of the oil-water mixture. Substituting Eqs. (9) and (10) into Eq. (8) yields:

$$c = \frac{1}{\sqrt{[Y_\mathrm{W}\rho_\mathrm{W} + (1 - Y_\mathrm{W})\rho_\mathrm{O}][Y_\mathrm{W}\kappa_\mathrm{W} + (1 - Y_\mathrm{W})\kappa_\mathrm{O}]}} \tag{11}$$

Thus, the water holdup can be solved by relating the ultrasonic sound velocity to the fluid medium density and average adiabatic compressibility.

Due to its simple formulation, the Urick model is applicable only to uniformly dispersed systems where interfacial effects are negligible. However, in viscoelastic fluids such as those containing polymers, its prediction accuracy is affected because it ignores interfacial slip, viscous effects, and the influence of dispersed phase particle size distribution.

6.2. Interfacial momentum transfer model

The IMT model shifts the research focus from the "bulk medium" to "individual dispersed phase particles". It holds that when sound waves propagate, there is relative motion between the dispersed phase particles and the continuous phase fluid; therefore, the particles are subjected to various interfacial forces, mainly including: Stokes viscous drag (F_{Stokes}) (Stokes (1851), which is the viscous frictional force caused by the relative velocity between the two phases; added mass force (F_A), which is the equivalent inertial force generated when the particles need to drive the surrounding fluid to accelerate together during their acceleration; Basset force ($F_{B,}$ also called history force) (Basset, 1888; Boussinesq, 1903), which is due to the viscosity of the fluid, when the particles are in unsteady motion (such as acceleration or deceleration), the development of the boundary layer on their surface depends on a time-dependent diffusion process, so the viscous drag exerted on the particles at a certain moment depends not only on the relative velocity at that moment but also on the entire acceleration history, reflecting the memory effect of fluid motion; and pressure gradient force (F_p), which is the force exerted on the particles due to their volume as a result of the pressure gradient in the sound field.Based on Basset's force equation; Net gravity force (F_G) refers to gravity minus buoyancy.

Tchen (1947) incorporated the pressure gradient force to derive the equation of motion for a particle in a flowing fluid in the vertical upward direction:

$$F = F_p + F_{\text{Stokes}} + F_A + F_B + F_G \tag{12}$$

where,

$$F = \frac{4}{3}\pi R^3 \rho_o \frac{du_o}{dt} \tag{13}$$

$$F_p = \frac{4}{3}\pi R^3 \rho_w \frac{du_w}{dt} \tag{14}$$

$$F_{\text{Stokes}} = -6\pi\mu_w R(u_o - u_w) \tag{15}$$

$$F_A = -\frac{2\pi R^3}{3}\rho_w \frac{d(u_o - u_w)}{dt} \tag{16}$$

$$F_B = -6\pi\mu_w R^2 \sqrt{\frac{\rho_w}{\pi\mu_w}} \int_{t_0}^{t} \frac{d(u_o(t_1) - u_w(t_1))}{\sqrt{t - t_1}dt} dt_1 \tag{17}$$

$$F_G = -\frac{4}{3}\pi R^3(\rho_o - \rho)g \tag{18}$$

where g is the gravitational acceleration; R is the particle radius; u_o and u_w are the velocities of the particle and fluid in the vertical direction, respectively; μ_w is the fluid viscosity.

The added mass force essentially represents the inertial effect of the fluid surrounding the particle being carried along when the particle accelerates. However, when the number of uniformly sized rigid particles increases, the volume of fluid that each particle can carry is affected by nearby particles. Therefore, Zuber (1964) addressed this issue by modifying the added mass force in the single-particle force analysis:

$$F_A = -\frac{2\pi R^3}{3}\rho_w \frac{1 + 2Y_o}{1 - Y_o} \frac{d(u_o - u_w)}{dt} \tag{19}$$

where Y_o is the particle volume fraction.

Harker and Temple (1988) studied the interaction of ultrasound with suspensions. Because ultrasound is a high-frequency continuous harmonic wave, the entire system is in a steady oscillatory state, and both the continuous and dispersed phases undergo high-frequency, sustained oscillations. In this case, the steady-state Stokes drag formula is no longer applicable, so they introduced a new Stokes oscillatory solution and a modified added mass force:

$$F_{\text{Stokes}} = 3\pi R^3 \omega\rho_w \left(\frac{1}{R}\sqrt{\frac{2\mu_w}{\omega\rho_w}} + \frac{2\mu_w}{\omega R^2 \rho_w}\right)(u_o - u_w) \tag{20}$$

$$F_A = -\frac{4\pi R^3}{3}\rho_w \left(\frac{1}{2}\frac{1 + 2Y_o}{1 - Y_o} + \frac{9}{4R}\sqrt{\frac{2\mu_w}{\omega\rho_w}}\right)\frac{d(u_o - u_w)}{dt} \tag{21}$$

where u_o and u_w are the oscillation velocities of the dispersed and continuous phases, respectively; ω is the ultrasonic frequency.

To further describe the microscopic oscillation behavior of droplets in an ultrasonic field, Harker and Temple treated the droplet as a sphere undergoing forced oscillation in the vertical direction within an acoustic field of frequency ω and wavelength λ. When at the wave peak position, u_o and u_w are greater than 0, direction is positive ($+z$ direction); when at the wave trough position, u_o and u_w are less than 0, direction is negative, as shown in Fig. 9. The velocity variations of the droplet and continuous phase under ultrasonic propagation oscillations are:

$$u_o = \overline{u}_o e^{i(kz - \omega t)}, u_w = \overline{u}_w e^{i(kz - \omega t)} \tag{22}$$

where $\overline{u}_o$ and $\overline{u}_w$ are the average oscillation amplitudes of the dispersed and continuous phases, respectively; k is the complex propagation constant, related to the ultrasonic propagation velocity, frequency, and attenuation during propagation.

As shown in Fig. 10, the simplified equation of motion in the vertical upward direction ($+z$ direction) is:

$$F = F_p + F_{\text{Stokes}} + F_A \tag{23}$$

where,

$$F = \frac{4}{3}\pi R^3 \rho_o \frac{du_o}{dt} \tag{24}$$

$$F_p = \frac{4}{3}\pi R^3 \frac{\partial p}{\partial z} \tag{25}$$

$$F_{\text{Stokes}} = 3\pi R^3 \omega\rho_w \left(\frac{1}{R}\sqrt{\frac{2\mu_w}{\omega\rho_w}} + \frac{2\mu_w}{\omega R^2 \rho_w}\right)(u_o - u_w) \tag{26}$$

$$F_A = -\frac{4\pi R^3}{3}\rho_w \left(\frac{1}{2}\frac{1 + 2Y_o}{1 - Y_o} + \frac{9}{4R}\sqrt{\frac{2\mu_w}{\omega\rho_w}}\right)\frac{d(u_o - u_w)}{dt} \tag{27}$$

The simplification is based on the characteristics of the high-frequency ultrasonic field: The Basset force (history force), originating from the memory effect due to the development of an unsteady boundary layer caused by fluid viscosity (Eq. (17)), is neglected because, under high-frequency oscillatory conditions,

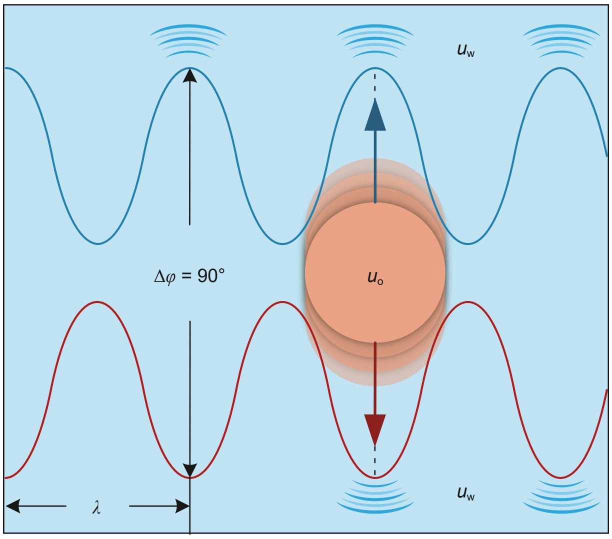

Fig. 9. Schematic diagram of droplet and fluid oscillation during ultrasonic propagation.

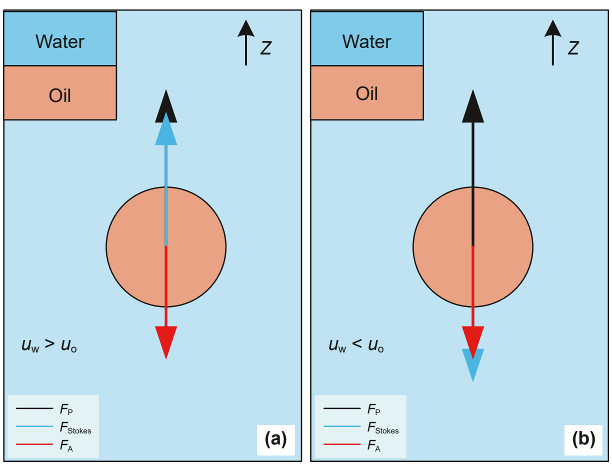

Fig. 10. Force balance equation on a particle in a fluid: (**a**) $u_w > u_o$; (**b**) $u_w < u_o$.

the droplet oscillation period is extremely short. The relaxation time for viscous diffusion far exceeds the oscillation period, rendering the magnitude of the historical force term F_B significantly smaller than that of the instantaneously responding Stokes drag force F_{Stokes}. The net gravity force F_G is a static force. In analyzing sound wave propagation velocity, the focus is on the high-frequency periodic oscillatory dynamics driven by the acoustic pressure gradient F_p. The influence of gravity within a single oscillation period is negligible compared to the relevant inertial and viscous forces, and it is therefore also omitted.

Substituting Eq. (22) into Eq. (23) allows obtaining the relationship between the dispersed phase velocity and the continuous phase velocity. Due to the high frequency of ultrasonic propagation, the droplet response can be considered as steady-state harmonic vibration. Thus, representing the velocity field in complex form facilitates solving the phase velocity relationship in the frequency domain:

$$u_o = \frac{B - iA}{B + iC} u_w \tag{28}$$

$$\begin{cases} A = \rho_w \left(\dfrac{1}{2} \dfrac{1 + 2Y_o}{1 - Y_o} + \dfrac{9}{4R} \sqrt{\dfrac{2\mu_w}{\omega \rho_w}} \right) \\ B = \dfrac{9}{4} \rho_w \left(\dfrac{1}{R} \sqrt{\dfrac{2\mu_w}{\omega \rho_w}} + \dfrac{2\mu_w}{\omega R^2 \rho_w} \right) \\ C = \rho_w - \rho_o - A \end{cases} \tag{29}$$

where, A is the added mass density term, characterizing the equivalent density of the surrounding fluid that needs to be mobilized when an oil droplet accelerates; B is the oscillatory drag coefficient, characterizing the damping effect of fluid viscosity on droplet motion; C is the net inertial density term, characterizing the net inertial density exhibited by the fluid itself.

Although the IMT transfer model can describe the force behavior of a single droplet at the microscopic level, its analytical perspective still has limitations. It primarily focuses on the force balance of a single droplet and fails to effectively establish a physical link between microscopic droplet vibration and macroscopic acoustic response, making it difficult to directly use for predicting the equivalent acoustic parameters of the mixed medium.

6.3. Development of the improved model

Based on the frequency-domain interfacial momentum theory proposed by Harker and Temple, this study introduces a key improvement through a unit control volume momentum conservation framework. This model framework starts from a microscopic control volume. By calculating the ratio of the total momentum flux to the total volumetric flow rate within the control volume, it derives the equivalent density of the entire mixed medium. This equivalent density is no longer a simple volume-weighted average but incorporates the physical results of interfacial slip and dynamic response.

To establish a physical connection between microscopic droplet forces, time-harmonic vibration, and the macroscopic acoustic response of the two-phase flow medium, this study introduces a control volume to extend the analysis scale from a single droplet to a control volume representing the entire system. Assume a pipeline cross-section has two rigid, weightless, infinitely parallel planes with a very small distance between them, filled with an oil-water mixture. Ultrasonic propagation causes the dispersed and continuous phases to undergo forced vibration in the vertical direction, as shown in Fig. 11.

Within a unit volume between the two planes, the volume fractions of the continuous phase and dispersed phase are Y_w and Y_o respectively, and $Y_w + Y_o = 1$. If the unit volume contained only moving continuous phase or dispersed phase medium, the density momentum of the medium at that time would be: $M_w' = \rho_w u_w$ or $M_o' = \rho_o u_o$, where M_w' and M_o' are the density momenta per unit volume of the continuous and dispersed phases, respectively. When the unit volume is filled with a moving oil-water mixture, the total density momentum is:

$$M' = Y_o \rho_o u_o + Y_w \rho_w u_w \tag{30}$$

The total volume flux u is:

$$u = Y_o u_o + Y_w u_w \tag{31}$$

The equivalent density of the oil-water two-phase flow is obtained by:

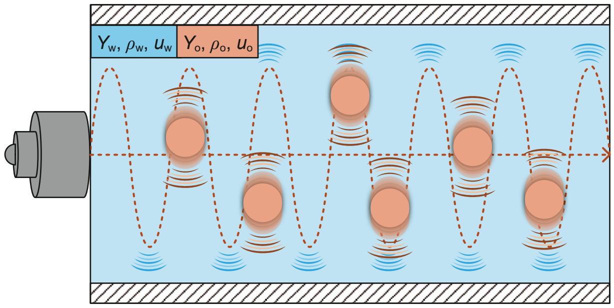

Fig. 11. Schematic diagram of the IMT model and its improvement.

$$\rho = \frac{M'}{u} = \frac{Y_o \rho_o u_o + Y_w \rho_w u_w}{Y_o u_o + Y_w u_w} \tag{32}$$

Through a control volume-based momentum conservation approach, the equivalent density of the mixture is derived as the ratio of total momentum flux to total volumetric flow rate, effectively incorporating interfacial slip effects beyond a simple volumetric average, thereby linking the microscopic phase velocities with the macroscopic sound velocity. Substituting Eq. (28) into Eq. (32) yields the equivalent density for the oil-water two-phase flow:

$$\rho = \frac{X^2B^2 + Y^2Z^2 + Y^2B^2 + X^2Z^2}{B^2 + Z^2} \tag{33}$$

Then, combining Eq. (33) with Eq. (10) and substituting into Eq. (8) gives the relationship between ultrasonic sound velocity and fluid medium density:

$$c = \frac{\sqrt{B^2 + Z^2}}{\sqrt{(Y_w \kappa_w + (1 - Y_w)\kappa_w)\left(X^2B^2 + Y^2Z^2 + Y^2B^2 + X^2Z^2\right)}} \tag{34}$$

where,

$$\begin{cases} X = \rho_w B Y_w + \rho_o B(1 - Y_w) \\ Y = \rho_w C Y_w - \rho_o A(1 - Y_w) \\ Z = A(1 - Y_w) - C Y_w \end{cases} \tag{35}$$

and

$$\begin{cases} A = \rho_w \left(\frac{1}{2}\frac{1 + 2Y_o}{1 - Y_o} + \frac{9}{4R}\sqrt{\frac{2\mu_w}{\omega \rho_w}} \right) \\ B = \frac{9}{4}\rho_w \left(\frac{1}{R}\sqrt{\frac{2\mu_w}{\omega \rho_w}} + \frac{2\mu_w}{\omega R^2 \rho_w} \right) \\ C = \rho_w - \rho_o - A \end{cases} \tag{36}$$

where, X is the macroscopic damping density term, characterizing the macroscopic viscous damping of the mixture; Y is the inertial coupling term, characterizing the competitive coupling between added mass and fluid inertia; Z is the phase lag intensity term, characterizing the inertial lag effect caused by the velocity phase difference between the two phases.

Table 2 defines the key parameters of the IIMT model and their physical meanings.

The added mass density term A increases with increasing viscosity and oil holdup, quantifying the equivalent inertial density effect generated when an oil droplet accelerates, i.e., the phenomenon of carrying the surrounding viscoelastic fluid. An increase in A indicates that droplet motion must overcome greater inertial resistance. The oscillatory drag coefficient B increases with increasing solution viscosity, meaning that high-viscosity NIPAS exert a stronger damping effect on the oscillatory motion of oil droplets, increasing the lag of droplet motion and reducing the oscillation amplitude, thus quantifying the microscopic interfacial resistance. The net inertial density term C is a coupling parameter that incorporates both macroscopic physical properties and microscopic dynamic effects. Its value decreases as the A term increases, clearly reflecting that the net inertial response of the continuous phase fluid is partially offset by the added mass effect.

The macroscopic damping density term X is the macroscopic manifestation of the B term weighted by holdup, characterizing the macroscopic equivalent viscous damping properties of the entire mixture. The inertial coupling term Y and the phase lag term Z together quantify the correction effect of interfacial slip on the macroscopic equivalent density. The Y term mainly reflects the amplitude change in equivalent density caused by slip, while the Z term directly quantifies the strength of the inertial lag effect caused by the velocity phase difference between the two phases.

Although the proposed IIMT model shows improved accuracy over conventional models, discrepancies with experimental data remain, mainly due to inherent simplifications. A key error source is the assumption of monodisperse, rigid spherical droplets, which contrasts with real polydisperse, deformable droplets in flow. Differently sized and shaped droplets respond variably to the acoustic field, causing systematic deviations. Additionally, the model's Newtonian framework neglects the viscoelasticity of polymer solutions, which alters droplet oscillation, coalescence, and breakup dynamics. Further discrepancy arises from spatial averaging by the ultrasonic transducer over non-uniform flows. The measured sound speed represents a path-integrated average across the aperture and pipe diameter, deviating from theoretical predictions, especially in inhomogeneous flow patterns such as D OS/W and D EOS/W.

Addressing these limitations outlines a clear path to advance the model from a conceptual framework to a robust practical tool. Theoretical refinement will involve incorporating viscoelastic constitutive models (e.g., Oldroyd-B or Giesekus) to capture fluid elasticity, introducing droplet size distribution functions to account for polydispersity and coalescence/breakup dynamics, and including shape correction factors for non-spherical droplets.

Table 2
Physical meaning of IIMT parameters.

Parameter	Physical meaning	Primary role
A	Added mass density term	Characterizes the equivalent density of fluid mobilized by accelerating droplets.
B	Oscillatory drag coefficient	Characterizes the viscous damping effect on droplet oscillation.
C	Net inertial density term	Characterizes the net inertial density of the continuous phase fluid
X	Macroscopic damping density term	Characterizes the macroscopic viscous damping of the mixture
Y	Inertial coupling term	Characterizes the coupling between added mass and fluid inertia
Z	Phase lag intensity term	Characterizes the inertial lag due to interphase velocity difference

Additionally, oscillatory shear rheometry will be used to obtain key viscoelastic parameters (e.g., complex modulus) for developing a frequency-domain force balance equation with viscoelastic coupling.

The model's applicability will be extended from vertical small-diameter pipes to industrially relevant conditions, including horizontal, inclined, and large-diameter flows, with careful consideration of gravitational effects on phase distribution and validation using field data or larger-scale experiments.

To further improve adaptability and accuracy, integrating data-driven methods with the physical model is a promising direction. This may include developing machine-learning classifiers for automated flow-pattern recognition from raw ultrasonic signals and establishing adaptive frameworks that map identified patterns to optimized model parameters, ultimately enabling a closed-loop, self-optimizing system for holdup prediction across all flow regimes.

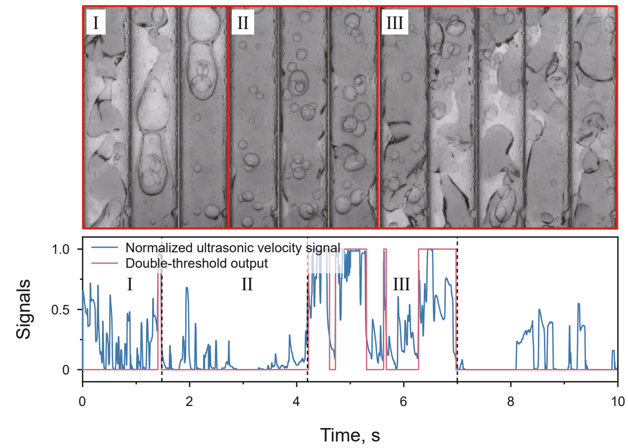

Fig. 12. Normalized sound velocity signal and output signal from the double-threshold method.

7. Water holdup prediction

The proposed IIMT model takes the experimentally measured ultrasonic sound velocity as its primary input. All water holdup predictions presented in this section are based on this experimental acoustic data and are subsequently validated against ground-truth measurements obtained via the quick-closing valve (QCV) technique. However, reliably extracting the sound velocity values used as model inputs from the raw acoustic signals first requires overcoming the challenges posed by the non-ideal signal characteristics resulting from complex flow patterns. In the experiments with polymer-containing oil-water two-phase flow, the presence of elongated slugs in the D EOS/W flow pattern causes the sound velocity signal sequence to include not only the signal of a complete cycle but also longer and more chaotic signals from oil slugs and transition periods, leading to errors in subsequent water holdup prediction. Therefore, to accurately extract the periodic signal of one water-slug/oil-slug cycle, it is necessary to distinguish between the continuous and dispersed phases beforehand. Thus, the self-adjusting double-threshold algorithm proposed by Welle (1985) was used to convert the original probe signal into a binary signal. The advantage of this method is its ability to adapt to signal baseline drift and amplitude changes. Research by Han et al. (2017) showed that the binarized signal processed by this method can clearly distinguish between oil and water phases, providing a reliable basis for subsequent analysis.

First, set the maximum value $\alpha_{\max}$, minimum value $\alpha_{\min}$, and the threshold α determined by signal fluctuations, which are continuously automatically adjusted based on the input signal sequence. Then, compare the value of the nth sample point Data(n) with the value of the ($n-1$)th sample point Data($n-1$) to determine the real-time $\alpha_{\max}$ and $\alpha_{\min}$. Subsequently, compare Data(n) with $\alpha_{\max}$ and $\alpha_{\min}$:

$$\mathrm{Data}(n) \leq \alpha_{\max} - \alpha \tag{37}$$

$$\mathrm{Data}(n) > \alpha_{\min} + \alpha \tag{38}$$

When condition (37) is met, the judgment result is 0, meaning oil is the continuous phase; when condition (38) is met, the judgment result is 1, meaning water is the continuous phase. Thus, the sound velocity signal sequence is converted into a 0-1 sequence. Then, combined with high-speed imaging, one cycle under the current flow condition is selected, as shown in Fig. 12. Regions II and III correspond to the oil slug and water slug, respectively, while Regions I and IV represent the chaotic flow patterns before the oil slug and after the water slug. The model is used to predict the water holdup under different continuous phases, and the overall water holdup prediction value for that flow condition is obtained by time-weighted averaging.

Based on the above preprocessing, the Urick model and the IIMT model were applied to predict the water holdup for 152 flow conditions covering 5 different flow patterns at 200 ppm and 152 flow conditions covering 4 different flow patterns at 1000 ppm. The prediction results were compared with the quick-closing valve measured values. Fig. 13 shows the comparison between the predicted and experimental water holdup values under 200 ppm and 1000 ppm conditions, where the vertical axis is the model-predicted value and the horizontal axis is the water holdup measured by the quick-closing valve.

By comparing Fig. 13(a) with (b), and Fig. 13(c) with (d), it can be seen that the IIMT model demonstrates higher prediction accuracy. Its advantage stems mainly from a more complete physical description of the interfacial forces, whereas the Urick model is based only on the idealized assumption of a homogeneous medium with no interaction between dispersed particles. This assumption corresponds to an extremely narrow range in the Oh–We parameter plane, requiring that inertial forces completely overcome surface tension to achieve uniform droplet breakup, while viscous forces are insufficient to cause droplet coalescence. Once the oil holdup increases or the flow velocity decreases, moving the flow into the D O/W or D LO/W regions, a decrease in We number or an increase in Oh number leads to droplet coalescence and non-uniform size distribution, invalidating the basic assumption of the Urick model and causing a significant increase in prediction error. Even under conditions close to its assumptions, this model still exhibits systematic deviation, manifested as the overall deviation of data points from the diagonal in Fig. 13(a).

The IIMT model, by introducing interfacial forces, considers to some extent the changes in the Oh number related to viscous effects and the influence of inertial effects, thus enabling a more accurate description of the two-phase flow dynamics environment under the combined action of Oh and We numbers. Therefore, even under flow conditions deviating from the homogeneity assumption, this model maintains high water holdup prediction accuracy over a wider range of Oh–We parameters.

By comparing Fig. 13(a) with (c), and Fig. 13(b) with (d), it can be observed that as the polymer concentration increases, the VFD O/W flow pattern disappears (under 1000 ppm conditions), and the water holdup prediction accuracy for all flow patterns under 1000 ppm conditions is better than that under 200 ppm.

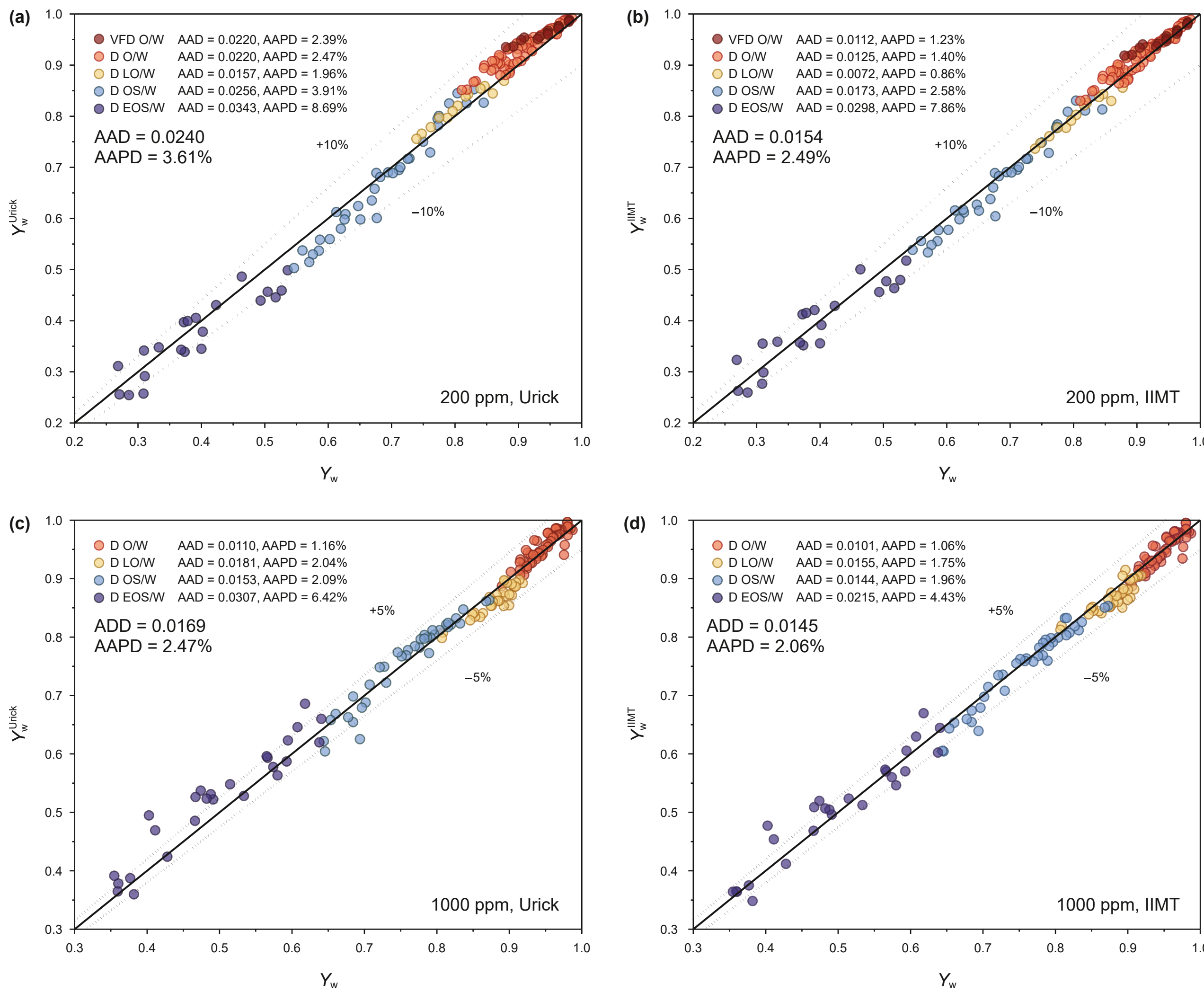

Fig. 13. Comparison of predicted water holdup and quick-closing valve experimental values: (**a**) 200 ppm, Urick; (**b**) 200 ppm, IIMT; (**c**) 1000 ppm, Urick; (**d**) 1000 ppm, IIMT.

Combined with the characteristics of the sound velocity signals, it is known that the high polymer concentration promotes oil droplet coalescence, reduces the number of fine oil bubbles, makes the oil droplet size distribution more uniform, and better aligns with the basic assumption of dispersed phase morphology in the IIMT model, significantly improving the prediction accuracy of water holdup.

Table 3 shows the prediction accuracy of each model under different polymer concentrations. It can be seen that at both 200 ppm and 1000 ppm, the IIMT model has the best prediction accuracy across different concentrations and flow patterns due to its more complete premises and consideration of forces. The Urick model, because it does not account for conditions like droplet coalescence in its assumptions, has the worst prediction accuracy.

Fig. 14 shows the distribution of the absolute error between the predicted values of the two types of models and the quick-closing valve measured values under 200 ppm and 1000 ppm conditions. The horizontal axis arranges different flow patterns in order of increasing mixture velocity and water cut. Overall, the errors under the 200 ppm concentration are generally higher than those under the 1000 ppm concentration. In the D OS/W and D EOS/W flow patterns, both models show significantly increased errors because their basic assumptions largely fail.

Under 200 ppm conditions, the errors for the VFD O/W and D O/W flow patterns generally show an increasing trend. The reason is that as the oil holdup increases, the mixture viscosity rises, leading to an increase in the Oh number, and the flow state gradually shifts from droplet breakup to droplet coalescence. Although viscous forces promote droplet coalescence and deformation, the polymer's limited ability to suppress turbulence at this concentration results in a relatively high We. This high inertial energy is sufficient to break up coalesced droplets, leading back to an uneven mixed state. Therefore, the uniform dispersion assumption relied upon by the Urick model and the equal-sized rigid particle assumption in the IIMT model gradually fail, leading to increasing errors. The IIMT model exhibits stronger robustness through the inclusion of various force terms; the viscous drag term slightly corrects for the deviation from the ideal assumption caused by coalescence; the added mass force and history force terms can, to some extent, respond to the differences in the high-frequency dynamic response of droplets of different sizes to the ultrasonic field, therefore the prediction error is generally smaller than that of the Urick model.

Under 1000 ppm conditions, the error for the D O/W flow pattern does not exhibit a significant increasing trend. The high Oh number resulting from the high polymer concentration significantly enhances the suppression of turbulence, the droplet resistance to deformation increases, the We number is insufficient to effectively break droplets, and the flow becomes more stable. Simultaneously, droplet coalescence accelerates under high

Table 3
Water holdup prediction accuracy (AAD/AAPD%) at 200 ppm and 1000 ppm.

Model	200 ppm, Urick	200 ppm, IIMT	1000 ppm, Urick	1000 ppm, IIMT
VFD O/W	0.0220/2.39	0.0112/1.23	—	—
D O/W	0.0220/2.47	0.0125/1.40	0.0110/1.16	0.0101/1.06
D LO/W	0.0157/1.96	0.072/0.86	0.0181/2.04	0.0155/1.75
D OS/W	0.0256/3.91	0.0173/2.58	0.0153/2.09	0.0144/1.96
D EOS/W	0.0343/8.69	0.0298/7.86	0.0307/6.42	0.0215/4.43
Total	0.0240/3.61	0.0154/2.49	0.0169/2.47	0.0145/2.06

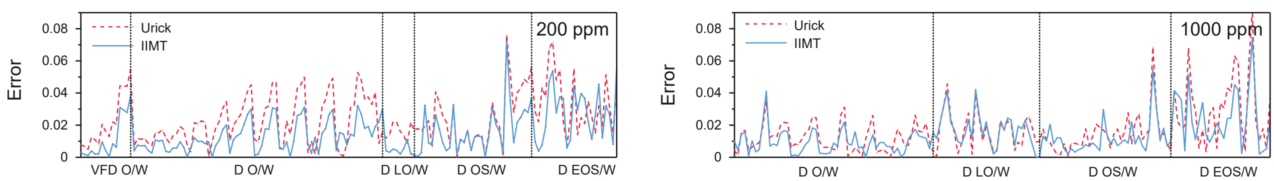

Fig. 14. Comparison of absolute errors between model-predicted water holdup and quick-closing valve measurements across flow patterns for 200 ppm and 1000 ppm conditions.

polymer concentration. Although coalescence leads to an increase in average size, the suppression of turbulence results in a more concentrated size distribution, closer to the model's ideal assumption, hence the error does not show an increasing trend.

Under 200 ppm conditions, the absolute error for the D LO/W flow pattern is instead lower than that at 1000 ppm. Combined with the Oh–We joint distribution map and high-speed camera analysis, at 200 ppm the Oh number is lower and the We number is higher; inertial forces still inhibit viscous coalescence to some extent, causing this flow pattern to appear under conditions of higher oil holdup and lower flow velocity, forming relatively concentrated and size-uniform cluster structures, closer to the model's basic assumption for dispersed phase morphology. When the polymer concentration increases to 1000 ppm, the Oh number increases significantly, the We number decreases, viscous forces dominate, turbulence suppression strengthens, the dispersed phase further coalesces, and the D LO/W flow pattern mostly appears under conditions of lower oil holdup and higher flow velocity. The oil bubble size distribution becomes more uneven, presenting a complex structure with mixed large and small oil bubbles, further deviating from the model's uniform sphere assumption, thus resulting in larger errors.

In the D OS/W and D EOS/W flow patterns, the errors show strong irregularity, mainly because under high oil holdup conditions, the basic assumptions of various models mostly no longer hold, leading to a significant increase in systematic deviation. Under 1000 ppm conditions, the prediction accuracy for the DOS O/W flow pattern is significantly better than that at 200 ppm. Combined with the Oh–We joint distribution map and high-speed camera analysis, the high-concentration NIPAS causes an increase in the Oh number, significantly suppressing turbulence intensity. The shape of the oil slugs becomes more regular, the boundaries clearer, reducing random rupture of the liquid film and droplet entrainment. This makes the alternation of oil slugs and water slugs more periodic, the oil bubble distribution in the water slug region more uniform, and the flow structure more stable. Therefore, although most assumptions of the IIMT model fail, the higher flow orderliness and phase distribution uniformity allow the model, based on equivalent medium theory, to still achieve better prediction results. Under 200 ppm conditions, the Oh number is lower, turbulence is still strong, oil bubble distribution within the liquid slug is uneven, and the liquid film is prone to instability and rupture, causing severe fluctuations in the sound velocity signal and increased model prediction deviation.

The IIMT model introduces the Stokes drag term to capture viscous effects; the added mass force and history force terms describe the dynamic response of the dispersed phase acceleration; the pressure gradient force term helps respond to sudden changes in the local flow field. Furthermore, by establishing a unit control volume momentum conservation framework, an expression for the equivalent density of the mixture medium is derived, establishing a physical link between microscopic interfacial interactions and macroscopic sound velocity response, thereby significantly enhancing the predictive capability for complex flow patterns. The Urick model, based on ideal assumptions of highly uniform dispersed phase and neglect of viscous and surface forces, sees its assumptions fail once the oil holdup increases into the D O/W flow pattern region, leading to poor water holdup prediction accuracy.

Based on the recurrence plot and probability density function analysis of the sound velocity signals: In the VFD O/W pattern, the PDF shows a narrow, high peak, and the recurrence plot shows uniformly distributed points; the Urick model assumptions hold, while the IIMT model corrects for the viscous resistance of tiny droplets, achieving the highest accuracy. In the D O/W pattern, the PDF is a broad peak, and the recurrence plot shows short diagonal clusters; in the D LO/W pattern, the PDF shows a main peak and a shoulder peak, and the recurrence plot has longer diagonal clusters; here, the Urick assumption fails, and the IIMT model captures oil bubble motion and droplet cluster abrupt changes through the added mass force and pressure gradient force, maintaining optimal accuracy. In the D OS/W pattern, the PDF is bimodal, and the recurrence plot shows a regular grid; in the D EOS/W pattern, the PDF is a bimodal distribution with a widened platform, and the recurrence plot shows large grids mixed with scattered points and short clusters; the Urick assumption completely fails. Although the IIMT model can describe oil slug slip and liquid film detachment, liquid film rupture still causes error fluctuations.

It should be noted that the interfacial momentum transfer model adopted in this study is based on the assumption of a Newtonian fluid. However, the polymer solution used in the experiments exhibits significant viscoelastic properties, which may lead to deviations between its actual rheological behavior and the model assumptions. Future research could further explore the incorporation of viscoelastic constitutive relations into the theoretical framework to more accurately describe the acoustic propagation characteristics of such complex fluids.

Regarding signal processing, the adaptive dual-threshold algorithm adopted in this study performs well under laboratory conditions with high signal-to-noise ratio ultrasonic signals, enabling clear discrimination between the oil and water phases and effective extraction of periodic signals. The algorithm achieves adaptive thresholding by dynamically adjusting local extremum values, demonstrating reliable performance with the high-quality experimental data obtained in this study. It must be acknowledged, however, that the performance of this mechanism may degrade when confronted with challenging conditions such as strong background noise, significant baseline drift, or severe signal amplitude fluctuations, all of which are commonly encountered in oilfield environments.

In the future, prior to practical application of the algorithm, advanced signal preprocessing techniques such as wavelet denoising and adaptive filtering will be integrated to enhance the raw signal quality, thereby improving the algorithm's stability and reliability in noisy environments. Furthermore, the validation in this study was based on an ultrasonic sensor with a center frequency of 2.25 MHz and specific experimental parameter ranges. Future work should systematically test the algorithm's adaptability using sensors with different center frequencies and bandwidths, and evaluate its performance across a wider range of flow velocities, holdup ratios, and polymer concentrations. This will allow for a comprehensive assessment of its universality and provide a basis for establishing parameter adaptation rules.

8. Conclusions

(1) Five distinct flow patterns were identified. Their transition is dictated by the shifting dominance among inertial, viscous, and surface tension forces, quantified by the We and Oh numbers. Increased polymer concentration raises mixture viscosity and the Ohnesorge number, suppressing turbulence, enhancing droplet coalescence, causing the disappearance of the VFD O/W pattern at 1000 ppm, and advancing the transition thresholds.

(2) The proposed IIMT model advances the classical interfacial momentum transfer theory by integrating a unit control volume momentum conservation framework. This innovation derives the equivalent density of the mixture from first principles, rigorously linking microscopic droplet forced oscillation and interfacial slip to the macroscopic sound velocity. It overcomes the critical limitations of the Urick model (which neglects interfacial interactions) and traditional IMT models (which lack a macro-scale acoustic coupling mechanism).

(3) Experimental validation confirms the IIMT model's significant superiority over the Urick model. For polymer concentrations of 200 ppm and 1000 ppm, the IIMT model achieved AAD of 0.0154 and 0.0145, and AAPD of 2.49% and 2.06%, respectively. Its incorporation of Stokes drag and added mass force provides enhanced robustness across complex, non-homogeneous flow patterns.

To advance the current model into a robust and widely applicable tool, future work will pursue three interconnected pathways: from a Newtonian to a viscoelastic formulation by incorporating constitutive models and population balance equations to capture fluid elasticity and droplet polydispersity; from laboratory to field conditions by extending validation to horizontal, inclined, and large-diameter pipes and testing with industrial flow data; and from a physical model to an intelligent hybrid system by integrating machine learning for automated flow pattern recognition and adaptive parameter optimization, thereby establishing a self-tuning predictive framework for complex multiphase flows.

CRediT authorship contribution statement

Feng Yue: Writing – original draft, Software, Investigation, Data curation. **Lan-Di Bai:** Writing – review & editing, Validation, Project administration, Investigation, Funding acquisition, Conceptualization. **Jia-Chen Zhang:** Visualization, Validation, Software, Formal analysis. **Zi-Yan Tang:** Visualization, Methodology, Investigation, Formal analysis. **Ning-De Jin:** Writing – review & editing, Validation, Resources, Project administration, Methodology, Investigation, Funding acquisition, Conceptualization.

Declaration of competing interest

The authors declare that they have no known competing financial interests or personal relationships that could have appeared to influence the work reported in this paper.

Acknowledgement

This work was supported by the National Natural Science Foundation of China (Grant Nos. 42374137, 52404035), the China Postdoctoral Science Foundation (Nos. 2024M762370, 2025T180799), the Graduate Program of Innovation in Arts and Sciences of Tianjin University (No. C1-2023-006).

References

Bai, B.J., Leng, J.Q., Wei, M.Z., 2022. A comprehensive review of in-situ polymer gel simulation for conformance control. Pet. Sci. 19 (1), 189–202. https://doi.org/10.1016/j.petsci.2021.09.043.
Basset, A.B., 1888. A Treatise on Hydrodynamics: with Numerous Examples. Deighton. Bell and Co., Cambridge.
Bonnet, J.C., Tavlarides, L.L., 1987. Ultrasonic technique for dispersed-phase holdup measurement. Ind. Eng. Chem. Res. 26 (4), 811–815. https://doi.org/10.1021/ie00064a032.
Boussinesq, J., 1903. Théorie Analytique De la chaleur: Mise en harmonie avec la thermodynamique et avec la théorie mécanique de la lumière, vol. 2. Gauthier-Villars, Paris.
Carvalho, R.D.M., Venturini, O.J., Tanahashi, E.I., et al., 2009. Application of the ultrasonic technique and high-speed filming for the study of the structure of air-water bubbly flows. Exp. Therm. Fluid Sci. 33 (7), 1065–1086. https://doi.org/10.1016/j.expthermflusci.2009.06.004.
Chen, X., Li, Y.Q., Liu, Z.Y., et al., 2023. Experimental investigation on the enhanced oil recovery efficiency of polymeric surfactant: matching relationship with core and emulsification ability. Pet. Sci. 20 (2), 619–635. https://doi.org/10.1016/j.petsci.2022.11.002.
Clarke, A., Howe, A.M., Mitchell, J., et al., 2016. How viscoelastic-polymer flooding enhances displacement efficiency. SPE J. 21 (3), 675–687. https://doi.org/10.2118/174654-pa.
Eckmann, J.P., Kamphorst, S.O., Ruelle, D., 1987. Recurrence plots of dynamical systems. Europhys. Lett. 4 (9), 973–977. https://doi.org/10.1209/0295-5075/4/9/004.
Evans, J.M., Attenborough, K., 1997. Coupled phase theory for sound propagation in emulsions. J. Acoust. Soc. Am. 102 (1), 278–282. https://doi.org/10.1121/1.419745.
Fan, J.H., Wang, F., 2021. Review of ultrasonic measurement methods for two-phase flow. Rev. Sci. Instrum. 92 (9), 091502. https://doi.org/10.1063/5.0049046.
Fang, L.D., Jia, H.J., Zheng, M., et al., 2025. Modelling and analysis of full-wavelength phase volume fraction measurement in liquid-solid two-phase flow. Energy 333, 137141. https://doi.org/10.1016/j.energy.2025.137141.
Harker, A.H., Temple, J.A.G., 1988. Velocity and attenuation of ultrasound in suspensions of particles in fluids. J. Phys. D Appl. Phys. 21 (11), 1576–1588. https://doi.org/10.1088/0022-3727/21/11/006.
Han, Y.F., Jin, N.D., Zhai, L.S., et al., 2017. Flow pattern and holdup phenomena of low velocity oil-water flows in a vertical upward small diameter pipe. J. Pet. Sci. Eng. 159, 387–408. https://doi.org/10.1016/j.petrol.2017.09.052.
Hinze, J.O., 1959. Turbulence: an Introduction to Its Mechanism and Theory. McGraw-Hill, New York.
Lamas, L.F., Botechia, V.E., Schiozer, D.J., et al., 2021. Application of polymer flooding in the revitalization of a mature heavy oil field. J. Pet. Sci. Eng. 204, 108695. https://doi.org/10.1016/j.petrol.2021.108695.

Lu, Z.K., Dupuis, E.D., Patel, V.K., et al., 2021. Ultrasonic oscillatory two-phase flow in microchannels. Phys. Fluids 33 (3), 032003. https://doi.org/10.1063/5.0039971.
Navaie, F., Esmaeilnezhad, E., Choi, H.J., 2022. Effect of rheological properties of polymer solution on flooding characteristics. Polymers 14 (24), 5555. https://doi.org/10.3390/polym14245555.
Rahiman, M.H.F., Rahim, R.A., Rahim, H.A., et al., 2013. Modelling ultrasonic sensor for gas bubble profiles characterization of chemical column. Sens. Actuators, B 184, 100–105. https://doi.org/10.1016/j.snb.2013.04.062.
Ren, W.K., Jin, N.D., Zhang, J.C., 2022. Modelling of ultrasonic method for measuring gas holdup of oil-gas-water three phase flows. Ultrasonics 124, 106740. https://doi.org/10.1016/j.ultras.2022.106740.
Rosado-Vázquez, F.J., Bashbush-Bauza, J.L., López-Ramírez, S., 2022. Practical mathematical model for the evaluation of main parameters in polymer flooding: rheology, adsorption, permeability reduction, and effective salinity. ACS Omega 7 (29), 24982–25002. https://doi.org/10.1021/acsomega.2c00277.
Seright, R.S., Wang, D., 2023. Polymer flooding: current status and future directions. Pet. Sci. 20 (2), 910–921. https://doi.org/10.1016/j.petsci.2023.02.002.
Seright, R.S., Brattekas, B., 2021. Water shutoff and conformance improvement: an introduction. Pet. Sci. 18 (2), 450–478. https://doi.org/10.1007/s12182-021-00546-1.
Stokes, G.G., 1851. On the effect of the internal friction of fluids on the motion of pendulums. Transactions of the Cambridge Philosophical Society 9, 8–106.
Stolojanu, V., Prakash, A., 1997. Hydrodynamic measurement in a slurry bubble column using ultrasonic techniques. Chem. Eng. Sci. 52 (21–22), 4225–4230. https://doi.org/10.1016/s0009-2509(97)00265-0.
Tan, F.Q., Ma, C.M., Qin, J.H., et al., 2022. Factors influencing oil recovery of surfactant-polymer flooding and establishment of a quantitative calculation model. Pet. Sci. 19 (3), 1198–1210. https://doi.org/10.1016/j.petsci.2022.01.001.
Takens, F., 1981. Detecting strange attractors in turbulence. In: Rand, D., Young, L.S. (Eds.), Dynamical Systems and Turbulence. Springer, Berlin, pp. 366–381. https://doi.org/10.1007/bfb0091924.
Tchen, C.M., 1947. Mean value and correlation problems connected with the motion of small particles suspended in a turbulent fluid. Delft University of Technology. Ph.D. thesis.
Urick, R.J., 1947. A sound velocity method for determining the compressibility of finely divided substances. J. Appl. Phys. 18 (11), 983–987. https://doi.org/10.1063/1.1697584.
Urick, R.J., Ament, W.S., 1949. The propagation of sound in composite media. J. Acoust. Soc. Am. 21 (2), 115–119. https://doi.org/10.1121/1.1917064.
Wang, Y., Zhang, J., Yang, S.L., et al., 2024. Pressure transient characteristics of non-uniform conductivity fractured wells in viscoelasticity polymer flooding based on oil-water two-phase flow. Pet. Sci. 21 (1), 343–351. https://doi.org/10.1016/j.petsci.2023.10.017.
Welle, R.V.D., 1985. Void fraction, bubble velocity and bubble size in two-phase flow. Int. J. Multiphas. Flow 11 (3), 317–345. https://doi.org/10.1016/0301-9322(85)90061-8.
Wood, A.B., 1930. A textbook of sound. G. Bell and Sons, London.
Xie, J.W., Zhu, P.F., Liu, Z.G., et al., 2024. Research on flow pattern identification model of oil-gas two-phase flow in scavenge pipe. Phys. Fluids 36 (6), 063317. https://doi.org/10.1063/5.0209397.
Xu, L.A., Leonard, D., Green, G., 1985. A pulsed ultrasound transducer system for two component flow. J. Sci. Instrum. 18 (7), 609–613. https://doi.org/10.1088/0022-3735/18/7/016.
Yang, H.Y., Wang, Y., Dai, Y., et al., 2023. On the acoustic attenuation characteristics of sonar detection in the salt-cavern gas storage environment. Front. Earth Sci. 10, 1029946. https://doi.org/10.3389/feart.2022.1029946.
Zhai, L.S., Jin, N.D., Gao, Z.K., et al., 2013. The ultrasonic measurement of high water volume fraction in dispersed oil-in-water flows. Chem. Eng. Sci. 94, 271–283. https://doi.org/10.1016/j.ces.2013.02.049.
Zhang, H., Guo, C.W., Lin, J., 2019. Effects of velocity profiles on measuring accuracy of transit-time ultrasonic flowmeter. Appl. Sci. 9 (8), 1648. https://doi.org/10.3390/app9081648.
Zhao, A., Han, Y.F., Ren, Y.Y., et al., 2016. Ultrasonic method for measuring water holdup of low velocity and high-water-cut oil-water two-phase flow. Appl. Geophys. 13 (1), 179–193. https://doi.org/10.1007/s11770-016-0547-z.
Zheng, Y., Zhang, Q.K., 2004. Simultaneous measurement of gas and solid holdups in multiphase systems using ultrasonic technique. Chem. Eng. Sci. 59 (17), 3505–3514. https://doi.org/10.1016/j.ces.2004.05.016.
Zhong, H.Y., Li, Y.Y., Zhang, W.D., et al., 2018. Microflow mechanism of oil displacement by viscoelastic hydrophobically associating water-soluble polymers in enhanced oil recovery. Polymers 10 (6), 628. https://doi.org/10.3390/polym10060628.
Zuber, N., 1964. On the dispersed two-phase flow in the laminar flow regime. Chem. Eng. Sci. 19 (11), 897–917. https://doi.org/10.1016/0009-2509(64)85067-3.